NANO LETTERS

Letter

pubs.acs.org/NanoLett

Proximity Band Structure and Spin Textures on Both Sides of Topological-Insulator/Ferromagnetic-Metal Interface and Their Charge Transport Probes

Juan Manuel Marmolejo-Tejada,[†,∥] Kapildeb Dolui,[†] Predrag Lazić,[‡] Po-Hao Chang,[¶] Søren Smidstrup,[§] Daniele Stradi,[§] Kurt Stokbro,[§] and Branislav K. Nikolić*[,†]

[†]Department of Physics and Astronomy, University of Delaware, Newark, Delaware 19716-2570, United States

[‡]Rudjer Bošković Institute, P.O. Box 180, Bijenička c. 54, 10 002 Zagreb, Croatia

[¶]Department of Physics and Astronomy, University of Nebraska Lincoln, Lincoln, Nebraska 68588, United States

[§]QuantumWise A/S, Fruebjergvej 3, Box 4, DK-2100 Copenhagen, Denmark

[∥]School of Electrical and Electronics Engineering, Universidad del Valle, Cali, AA 25360, Colombia

ABSTRACT: The control of recently observed spintronic effects in topological-insulator/ferromagnetic-metal (TI/FM) heterostructures is thwarted by the lack of understanding of band structure and spin textures around their interfaces. Here we combine density functional theory with Green's function techniques to obtain the spectral function at any plane passing through atoms of Bi_2Se_3 and Co or Cu layers comprising the interface. Instead of naively assumed Dirac cone gapped by the proximity exchange field spectral function, we find that the Rashba ferromagnetic model describes the spectral function on the surface of Bi_2Se_3 in contact with Co near the Fermi level E_F^0, where circular and snowflake-like constant energy contours coexist around which spin locks to momentum. The remnant of the Dirac cone is hybridized with evanescent wave functions from metallic layers and pushed, due to charge transfer from Co or Cu layers, a few tenths of an electron-volt below E_F^0 for both Bi_2Se_3/Co and Bi_2Se_3/Cu interfaces while hosting distorted helical spin texture wounding around a single circle. These features explain recent observation of sensitivity of spin-to-charge conversion signal at TI/Cu interface to tuning of E_F^0. Crucially for spin−orbit torque in TI/FM heterostructures, few monolayers of Co adjacent to Bi_2Se_3 host spectral functions very different from the bulk metal, as well as in-plane spin textures (despite Co magnetization being out-of-plane) due to proximity spin−orbit coupling in Co induced by Bi_2Se_3. We predict that out-of-plane tunneling anisotropic magnetoresistance in Cu/Bi_2Se_3/Co vertical heterostructure can serve as a sensitive probe of the type of spin texture residing at E_F^0.

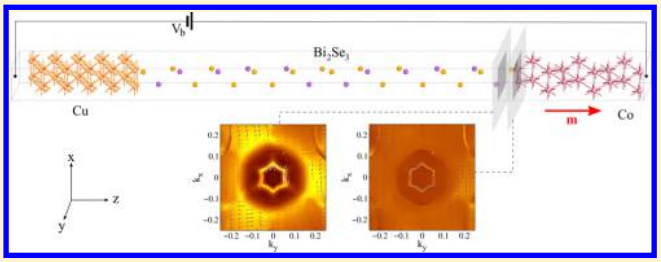

KEYWORDS: *Topological insulators, ultrathin ferromagnetic layers, spin−orbit proximity effect, spintronics, tunneling anisotropic magnetoresistance, first-principles calculations*

The recent experiments on spin−orbit torque (SOT)[1−4] and spin-to-charge conversion[5−10] in topological-insulator/ferromagnetic-metal (TI/FM) heterostructures[11,12] have ignited the field of topological spintronics. In these heterostructures, giant nonequilibrium spin densities[13−16] are expected to be generated due to strong spin−orbit coupling (SOC) on metallic surfaces of three-dimensional (3D) TIs and the corresponding (nearly[17]) helical spin-momentum locking along a single Fermi circle for Dirac electrons hosted by those surfaces.[11,12] Such strong interfacial SOC-driven phenomena are also envisaged to underlie a plethora of novel spintronic technologies.[18]

The theoretical interpretation of these effects has thus far relied almost exclusively on plausible simplistic models of TI/FM interface, such as the Dirac Hamiltonian with an additional Zeeman term describing coupling of magnetization of the FM layer to the surface state spins,[11,12] $\hat{H}^{\mathrm{Dirac}} = v_F\ (\hat{\boldsymbol{\sigma}} \times \hat{\mathbf{p}})_z - \Delta\ \mathbf{m}\cdot\hat{\boldsymbol{\sigma}}$, where $\hat{\mathbf{p}}$ is the momentum operator, $\hat{\boldsymbol{\sigma}}$ is the vector of the Pauli matrices, $\mathbf{m}$ is the unit vector along the magnetization direction, and v_F is the Fermi velocity. Thus, the only effect of the FM layer captured by $\hat{H}^{\mathrm{Dirac}}$ is proximity effect-induced exchange coupling Δ which opens a gap in the Dirac cone energy-momentum dispersion,[11,12] thereby making Dirac electrons massive. On the other hand, recent first-principles calculations[20,21] have demonstrated that band structure of even TI/ferromagnetic-insulator (TI/FI) bilayers, where hybridization between TI and FI states is largely absent, cannot be captured by simplistic models like $\hat{H}^{\mathrm{Dirac}}$. The properties of TI/FM interfaces are far more complex due to penetration of evanescent wave functions from the FM layer into the bulk gap of the TI layer, which can hybridize with surface state of TI and

Received: June 14, 2017
Revised: August 9, 2017
Published: August 10, 2017

DOI: 10.1021/acs.nanolett.7b02511
Nano Lett. 2017, 17, 5626−5633

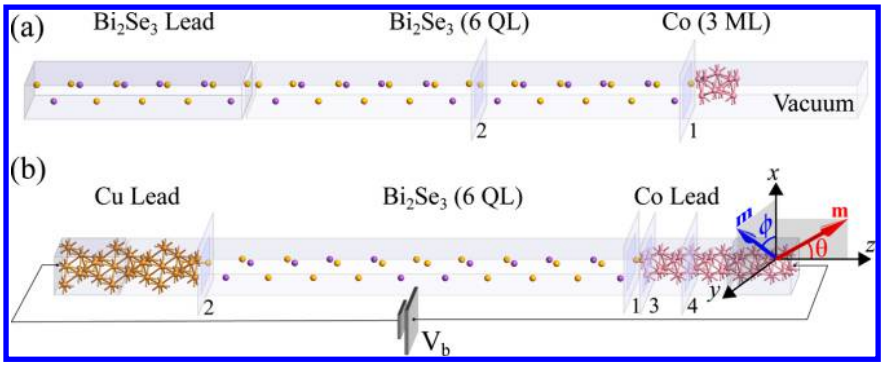

Figure 1. Schematic view of TI-based heterostructures where (a) semi-infinite Bi_2Se_3(111) layer is attached to n monolayers of Co(0001); (b) 6 QLs of Bi_2Se_3 are sandwiched between semi-infinite Cu(111) layer and semi-infinite Co(0001) layer. Both heterostructures are infinite in the transverse direction, so that the depicted supercells are periodically repeated within the xy-plane. The magnetization **m** of the Co layer is fixed along the z-axis in (a), or rotated within the xy-plane or the xz-plane in (b). Applying the bias voltage V_b to the vertical heterostructure in panel (b) leads to a charge current flowing perpendicularly to both Bi_2Se_3/Cu and Bi_2Se_3/Co interfaces.

blur its Dirac cone (as already observed in tight-binding models of TI/normal-metal interfaces[15,22,23]), as well as related charge transfer. Thus, the key issue for topological spintronics[1−10,18] is to understand band structure and spin textures (including the fate of the Dirac cone and its spin-momentum locking) in hybridized TI with FM or normal metal (NM)[10] layers at nanometer scale around the interface where they are brought into contact; the properties of both TI side and FM or NM side of the interface can be quite different from the properties of corresponding bulk materials.

For example, computational searches[19] for new materials realizing 3D TIs (or other topologically nontrivial electronic phases of matter-like Weyl semimetals[24] and Chern insulators[25]) have crucially relied on first-principles calculations of spectral function on their boundaries and its confirmation by spin- and angle-resolved photoemission spectroscopy (spin-ARPES).[26] A standard density functional theory (DFT)-based framework developed for this purpose, where DFT band structure around the Fermi level E_F^0 is reconstructed using the Wannier tight-binding Hamiltonian,[27] which is then employed to obtain the retarded Green's function (GF) of semi-infinite homogeneous crystal and the spectral function on its surface in contact with vacuum,[19,24,25] is difficult to apply to complicated inhomogeneous systems like TI/FM bilayers due to strongly entangled bands in the region of interest around E_F^0. Also, spin-ARPES experiments cannot probe buried interfaces below too many monolayers (e.g., penetration depth of low-energy photons is 2−4 nm) of FM or NM deposited onto the TI surface.[26]

An attempt[28] to obtain the spectral function, $A_j(E;\mathbf{k}) = \sum_{n,i}^{i\in \mathrm{QL}_j} w_{n\mathbf{k}}^i\, \delta(E - \varepsilon_{n\mathbf{k}})$, directly from DFT-computed energy-momentum dispersion $\varepsilon_{n\mathbf{k}}$ (n is the band index and $\mathbf{k}$ is the crystal momentum) and site-projected character $w_{n\mathbf{k}}^i$ of the corresponding eigenfunctions for TI/FM supercells has produced ambiguous results. This is due to arbitrariness in broadening the delta function $\delta(E - \varepsilon_{n\mathbf{k}})$, as well as due to usage of atomic sites i within the whole jth quintuple layer (QL_j) of Bi_2Se_3 (one QL consists of three Se layers strongly bonded to two Bi layers in between) which effectively averages the spectral functions over all geometric planes within QL_j. Similar ambiguities (such as setting the amount of electron density that is localized on the surface or within the whole interfacial QL) plague interpretation of the so-called projected DFT band structure of TI/FI[21] and TI/FM[29] bilayers.

In this Letter, we develop a framework that combines the noncollinear DFT Hamiltonian $\mathbf{H}^{\mathrm{DFT}}$, represented in a basis of variationally optimized localized atomic orbitals[30] with retarded GF calculations from which one can extract the spectral function and spin textures at an arbitrary geometric plane of interest within a junction combining TI, FM, and NM layers (note that related effort was made in ref 31 but it was applied only to surfaces of semi-infinite homogeneous crystals rather than interfaces in the focus of our study). It also makes it possible to compute their spin and charge transport properties in the linear-response regime or at finite bias voltage. It is worth mentioning that our $\mathbf{H}^{\mathrm{DFT}}$ computed from pseudopotential-based DFT is as accurate[14] for describing TIs as widely used[17] projector augmented wave[32] (PAW) method-based DFT where $\mathbf{H}^{\mathrm{DFT}}$ is represented in the basis of plane waves. We apply this framework to two Bi_2Se_3-based heterostructures whose supercells are depicted in Figure 1, where we assume that those supercells are periodically repeated in the transverse xy-direction.

The heterostructure in Figure 1a consists of Bi_2Se_3, chosen as the prototypical 3D TI,[11,12,17,19] whose surface is covered by n monolayers (MLs) of Co. The retarded GF of this heterostructure is computed as

$$\mathbf{G}_{\mathbf{k}_\parallel}(E) = [E - \mathbf{H}_{\mathbf{k}_\parallel}^{\mathrm{DFT}} - \mathbf{\Sigma}_{\mathbf{k}_\parallel}^{\mathrm{Bi_2Se_3}}(E)]^{-1} \tag{1}$$

where $\mathbf{k}_\parallel = (k_x, k_y)$ is the transverse k-vector, $\mathbf{\Sigma}_{\mathbf{k}_\parallel}^{\mathrm{Bi_2Se_3}}(E)$ is the self-energy[33−35] describing the semi-infinite Bi_2Se_3 lead and $\mathbf{H}_{\mathbf{k}_\parallel}^{\mathrm{DFT}}$ is the Hamiltonian of the active region consisting of n MLs of cobalt plus six QLs of Bi_2Se_3 to which the lead is attached. We choose n = 1−3 because ultrathin FM layers of thickness ≃1 nm are typically employed in SOT experiments[36] in order to preserve perpendicular magnetic anisotropy (note that magnetocrystalline anisotropy does favor out-of-plane **m** in Bi_2Se_3/Co bilayers[29]). The spectral function (or local density of states) at an arbitrary plane at position z within the active region is computed from

$$A(E;\, k_x,\, k_y,\, z) = -\frac{1}{\pi}\,\mathrm{Im}[G_{\mathbf{k}_\parallel}(E;\, z,\, z)] \tag{2}$$

where the diagonal matrix elements $G_{\mathbf{k}_\parallel}(E;\, z,\, z)$ are obtained by transforming eq 1 from orbital to a real-space representation.

The heterostructure in Figure 1b consists of semi-infinite Cu and Co leads sandwiching a Bi_2Se_3 layer of finite thickness,

DOI: 10.1021/acs.nanolett.7b02511
Nano Lett. 2017, 17, 5626−5633

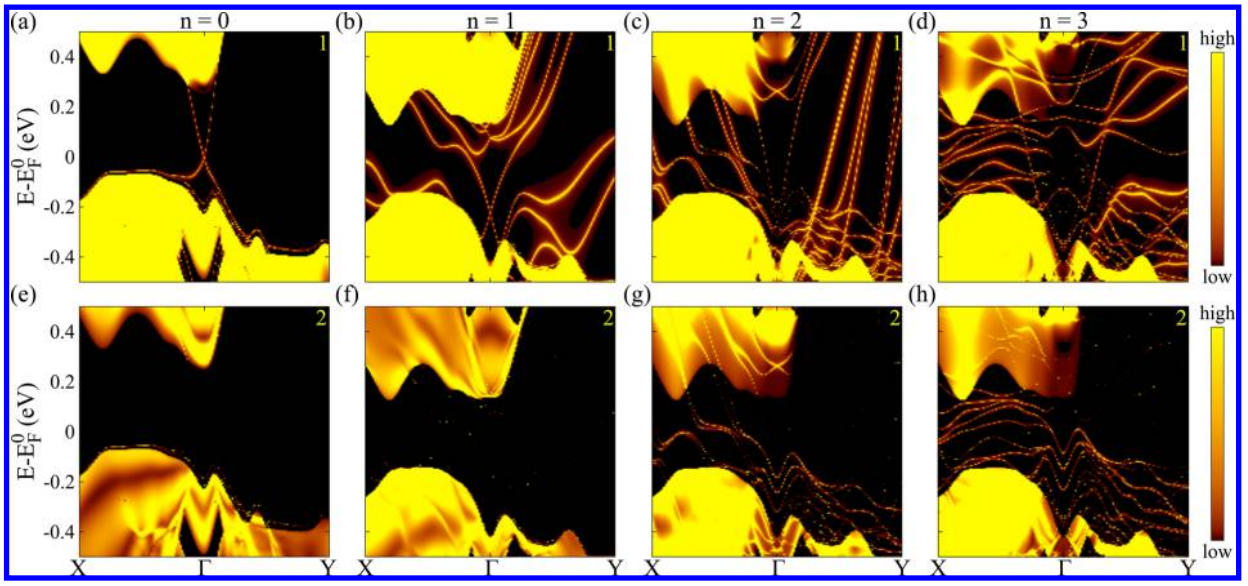

Figure 2. Spectral function, defined in eq 2, at plane 1 for panels b–d or plane 2 for panels f–h within Bi_2Se_3/Co(n ML) heterostructure in Figure 1a with $\mathbf{m} \parallel \hat{z}$. For comparison, panels a and e plot the spectral function at planes 1 (akin to ref 19) and 2, respectively, within semi-infinite Bi_2Se_3 crystal in contact with vacuum (i.e., $n = 0$). From Γ to Y we plot $A(E; k_x = 0, k_y; z \in \{1,2\})$, whereas from Γ to X we plot $A(E; k_x, k_y = 0; z \in \{1,2\})$.

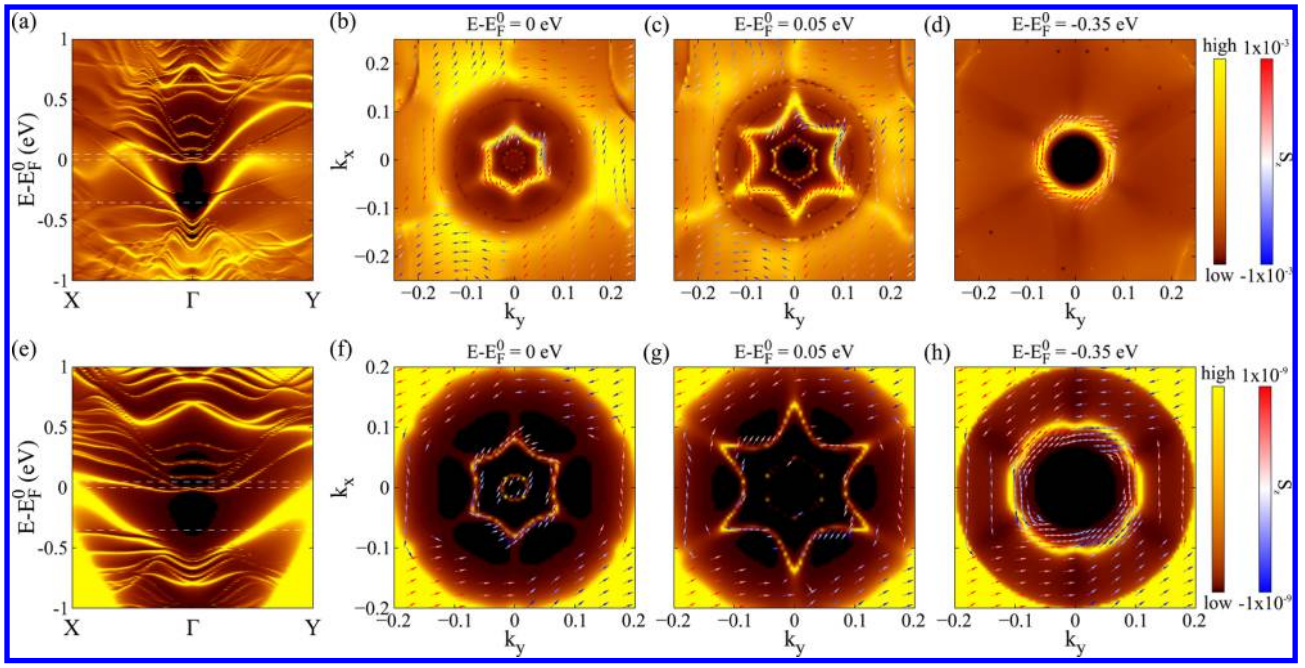

Figure 3. Spectral function at (a–d) plane 1 in Figure 1b which is passing through Se atoms at the Bi_2Se_3/Co interface with $\mathbf{m} \parallel \hat{z}$; and (e–h) plane 2 in Figure 1b which is passing through Se atoms at Bi_2Se_3/Cu interface, where we remove Co layer to make Bi_2Se_3 semi-infinite along the z-axis. In panels a,e, we plot $A(E; k_x = 0, k_y; z \in \{1,2\})$ from Γ to Y and $A(E; k_x, k_y = 0; z \in \{1,2\})$ from Γ to X. Panels b–d and f–h plot constant energy contours of $A(E - E_F^0 \in \{0.0, 0.05, -0.35 \text{ eV}\}; k_x, k_y; z \in \{1,2\})$ at three energies marked by horizontal dashed lines in panels a or e, respectively, as well as the corresponding spin textures where the out-of-plane S_z component is indicted in color (red for positive and blue for negative). The units for k_x and k_y are $2\pi/a$ where a is the lattice constant of a common supercell combining two unit cells of the two layers around the corresponding interface.

where we choose Cu as the NM layer similar to the very recent spin-to-charge conversion experiment of ref 10. Such a heterostructure is termed vertical or current-perpendicular-to-plane in spintronics terminology because applying bias voltage V_b drives a current perpendicularly to the TI/FM interface. Its retarded GF is computed as

$$\mathbf{G}_{\mathbf{k}_\parallel}(E) = [E - \mathbf{H}_{\mathbf{k}_\parallel}^{\mathrm{DFT}} - \mathbf{\Sigma}_{\mathbf{k}_\parallel}^{\mathrm{Cu}}(E) - \mathbf{\Sigma}_{\mathbf{k}_\parallel}^{\mathrm{Co}}(E)]^{-1} \quad (3)$$

where $\mathbf{H}_{\mathbf{k}_\parallel}^{\mathrm{DFT}}$ describes the active region consisting of six QLs of Bi_2Se_3 plus four MLs of Cu and four MLs of Cu. Its linear-response resistance R is given by the Landauer formula

$$\frac{1}{R} = \frac{e^2}{h\Omega_{\mathrm{BZ}}} \int_{\mathrm{BZ}} \mathrm{d}\mathbf{k}_\parallel \int \mathrm{d}E \left(-\frac{\partial f}{\partial E}\right) \mathrm{Tr}[\mathbf{\Gamma}_{\mathbf{k}_\parallel}^{\mathrm{Co}} \mathbf{G}_{\mathbf{k}_\parallel} \mathbf{\Gamma}_{\mathbf{k}_\parallel}^{\mathrm{Cu}} \mathbf{G}_{\mathbf{k}_\parallel}^{\dagger}] \quad (4)$$

where we assume temperature T = 300 K in the Fermi–Dirac distribution function $f(E)$, $\mathbf{\Gamma}_{\mathbf{k}_\parallel}^{\alpha} = i(\mathbf{\Sigma}_{\mathbf{k}_\parallel}^{\alpha} - [\mathbf{\Sigma}_{\mathbf{k}_\parallel}^{\alpha}]^{\dagger})$ and Ω_{BZ} is the

DOI: 10.1021/acs.nanolett.7b02511
Nano Lett. 2017, 17, 5626–5633

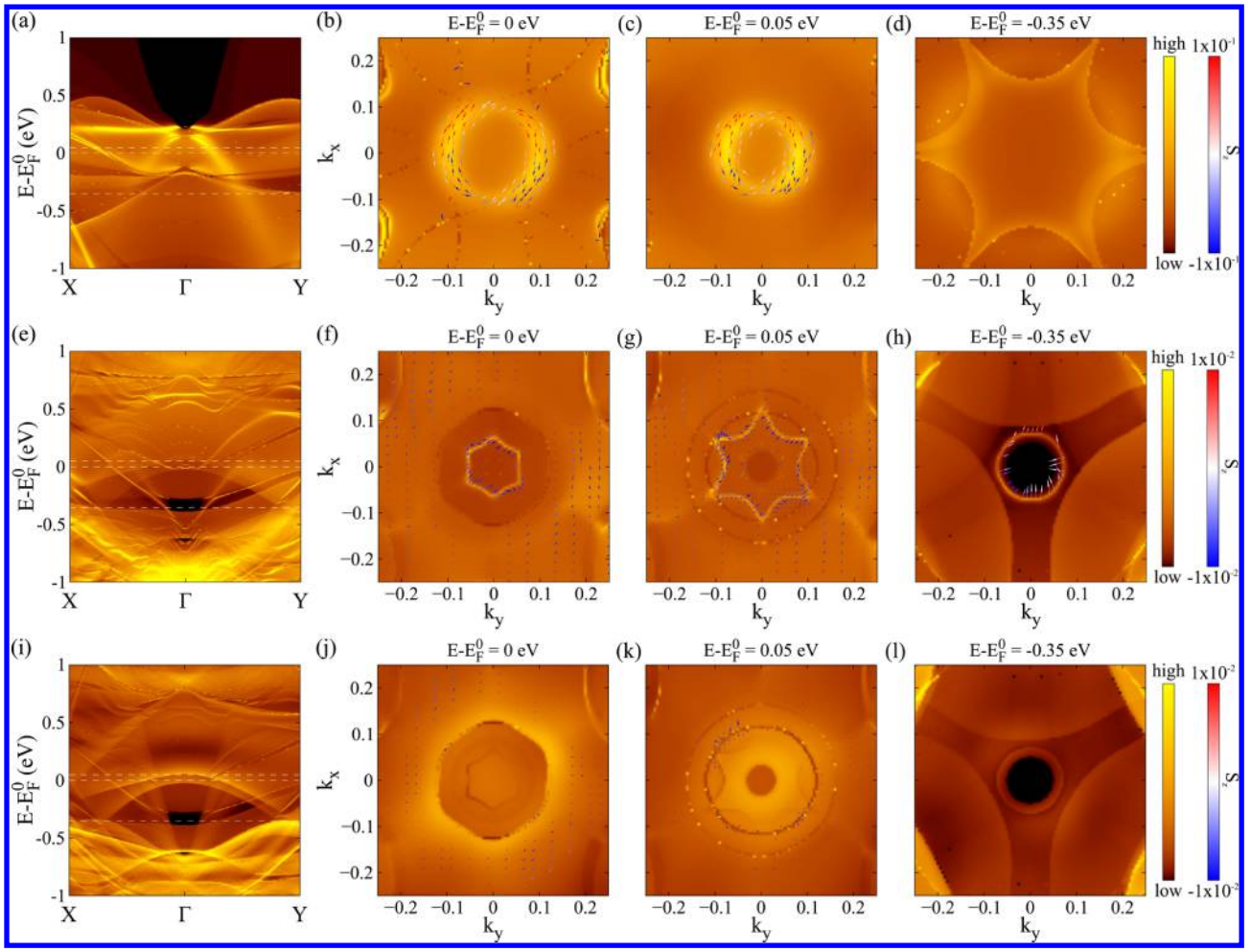

Figure 4. Spectral function at (a–d) the surface of a semi-infinite Co layer in contact with vacuum; (e–h) plane 3 in Figure 1b passing through Co atoms at the Bi_2Se_3/Co interface; and (i–l) plane 4 in Figure 1b passing through Co atoms away from the interface. Magnetization **m** of Co layer is perpendicular to the interface, $\mathbf{m} \parallel \hat{z}$, in all panels a–l. In panels e and i, we plot $A(E; k_x = 0, k_y; z \in 3)$ from Γ to *Y* and $A(E; k_x, k_y = 0; z \in 3)$ from Γ to *X*. Panels b–d, f–h, and j–l plot constant energy contours of the spectral function at three energies marked by horizontal dashed lines in panels a, e, and i, respectively, as well as the corresponding spin textures where the magnitude of the out-of-plane S_z component is indicted in color (red for positive and blue for negative). The units for k_x and k_y are $2\pi/a$ where *a* is the lattice constant of a common supercell combining two unit cells of the two layers around the corresponding interface.

area of the two-dimensional (2D) Brillouin zone (BZ) within which $\mathbf{k}_\parallel$ vectors are sampled.

The spectral function of the heterostructure in Figure 1a computed at planes 1 and 2 within the Bi_2Se_3 layer is shown in Figure 2b–d and f–h, respectively, where plane 1 is passing through Se atoms on the Bi_2Se_3 surface in contact with Co layer and plane 2 is three QLs (or ≃2.85 nm) away from plane 1. For comparison, we also show in Figure 2a,b the spectral function at the same two planes within the semi-infinite Bi_2Se_3 layer in contact with vacuum, thereby reproducing the results from ref 19 by our formalism. While the Dirac cone at the Γ-point is still intact in Figure 2b for $n = 1$ ML of Co, its Dirac point (DP) is gradually pushed into the valence band of Bi_2Se_3 with increasing *n* because of charge transfer from metal to TI. The charge transfer visualized in Figure 6c,d is relatively small, but due to small density of states (DOS) at the DP it is easy to push it down until it merges with the larger DOS in the valence band of the TI. Adding more MLs of Co in Figure 2c,d also introduces additional bands within the bulk gap of Bi_2Se_3 due to penetration of evanescent wave functions that hybridize with the Dirac cone. The metallic surface states of Bi_2Se_3 itself penetrate into its bulk over a distance of two QLs,[14] so that in Figure 2e the spectral function on plane 2 vanishes inside the gap of the semi-infinite Bi_2Se_3 layer in contact with vacuum, while the remaining states inside the gap in Figure 2f–h can be attributed to the Co layer.

For infinitely many MLs of Co attached to six QLs of Bi_2Se_3 within the Cu/Bi_2Se_3/Co heterostructure in Figure 1(b), the remnant of the Dirac cone from the TI surface can be identified in Figure 3a at around 0.5 eV below E_F^0 while it is pushed even further below in the case of Cu/Bi_2Se_3 interface in Figure 3e. The difference in work functions $\Phi_{Co} = 5.0$ eV or $\Phi_{Cu} = 4.7$ eV and electron affinity $\chi_{Bi_2Se_3} = 5.3$ eV determines[28] the band alignment and the strength of hybridization, where *n*-type doping [see also Figure 6c,d] of the Bi_2Se_3 layer pins E_F^0 of the whole Cu/Bi_2Se_3/Co heterostructure in the conduction band of the bulk Bi_2Se_3. The remnant of the Dirac cone is quite different from the often assumed[11,12] eigenspectrum of $\hat{H}^{Dirac}$ because of hybridization with the valence band of Bi_2Se_3, as well as with evanescent states originating from Co or Cu layers whose penetration into TI is visualized by plotting position- and energy-dependent spectral function

DOI: 10.1021/acs.nanolett.7b02511
Nano Lett. 2017, 17, 5626–5633

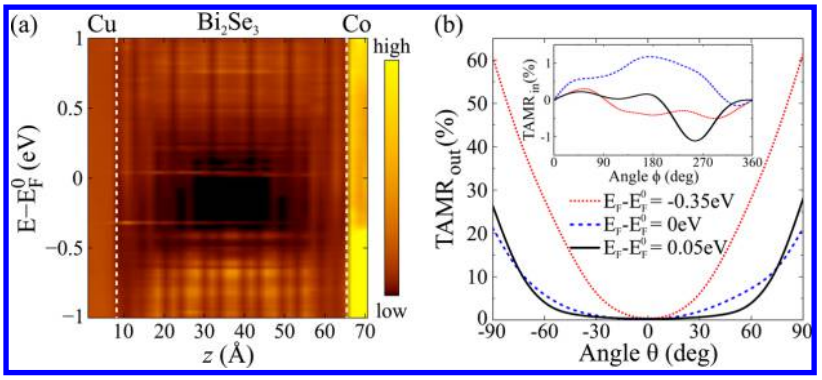

Figure 5. (a) The position- and energy-dependent spectral function $A(E; z)$, defined in eq 5, from the left Cu lead, across Bi_2Se_3 tunnel barrier, toward the right Co lead for the heterostructure in Figure 1b. (b) The out-of-plane $TAMR_{out}(\theta)$ ratio defined in eq 6 as a function of angle θ between the magnetization $\mathbf{m}$ and the direction of current injected along the z-axis in Figure 1b. Inset in panel b shows angular dependence of the in-plane $TAMR_{in}(\phi)$ ratio. In order to converge the integration over the transverse wave vector $\mathbf{k}_\parallel$ in eq 4, we employ a uniform grid of 101 × 101 k-points for $TAMR_{out}(\theta)$ and 251 × 251 k-points for $TAMR_{in}(\phi)$.

$$A(E; z) = \frac{1}{\Omega_{BZ}} \int dk_x dk_y A(E; k_x, k_y; z) \tag{5}$$

in Figure 5a. On the other hand, the energy-momentum dispersion in the vicinity of E_F^0 and for an interval of $\mathbf{k}_\parallel$ vectors around the Γ-point is surprisingly well-described by another simplistic model—ferromagnetic Rashba Hamiltonian.[37]

In Figure 3b–d and f—h, we show constant energy contours of the spectral function at three selected energies E denoted in Figure 3a,e by dashed horizontal lines. Instead of a single circle as the constant energy contour for the eigenspectrum of $\hat{H}^{Dirac}$, or single hexagon or snowflake-like contours (due to hexagonal warping[17]) sufficiently away from DP for the eigenspectrum of $\mathbf{H}^{DFT}$ of the isolated Bi_2Se_3 layer, here we find multiple circular and snowflake-like contours close to the Γ-point. The spin textures within the constant energy contours are computed from the spin-resolved spectral function. For energies near $E = E_F^0$, the spin textures shown in Figure 3b,c are quite different from the helical ones in isolated Bi_2Se_3 layer.[19] Nevertheless, Figure 3d shows that the remnant Dirac cone still generates distorted helical spin texture wounding along a single circle but with out-of-plane S_z component due to the presence of Co layer.

The envisaged applications of TIs in spintronics are based[1−10,13,15,16] on spin textures like the one in Figure 3d because it maximizes[13,14] generation of nonequilibrium spin density when current is passed parallel to the TI surface. However, utilizing spin texture in Figure 3d in lateral TI/FM heterostructures would require to shift E_F (by changing the composition of TI[10] or by applying a gate voltage[4]) by few tenths of an electron-volt below E_F^0 of the undoped heterostructures in Figure 3a. For example, extreme sensitivity of spin-to-charge conversion was recently observed in ref 10 on the surface of $(Bi_{1-x}Sb_x)_2Te_3$ covered by a 8 nm thick Cu layer as E_F of the TI layer was tuned, which is difficult to explain by assuming that the Dirac cone on the TI surface remains intact after the deposition of the Cu layer (e.g., ref 10 had to invoke "instability of the helical spin structure"). On the other hand, it becomes easy to explain using Figure 3f–h that demonstrates how spin textures at Bi_2Se_3/Cu interface change dramatically as one moves E_F (even slightly) below or above E_F^0. Comparing Figure 3a–d with e–h makes it possible to understand the effect of the magnetization of the Co layer, which modifies[37] the Rashba dispersion around E_F^0 and the corresponding spin textures (particularly the out-of-plane S_z component).

The theoretical modeling of SOT in TI/FM[1,16] or heavy-metal/FM[38] bilayers is usually conducted by starting from strictly 2D Hamiltonians, such as $\hat{H}^{Dirac}$ or the Rashba ferromagnetic model,[37] respectively, so that the FM layer is not considered explicitly. Figure 4f–h shows that this is not warranted because the Bi_2Se_3 layer induces proximity SOC and the corresponding proximity in-plane spin textures over the few MLs of Co, which decay to negligible values in Figure 4j–l only after reaching plane 4 in Figure 1b. The fact that conventional room-temperature metallic ferromagnet can acquire properties of nearby TI, as demonstrated convincingly by Figure 4e–l solves the problem of very small critical temperature $\lesssim$10 K in recent attempts[2,39] to create ferromagnetic topological matter by doping 3D TIs with magnetic impurities. The existence of proximity in-plane spin textures in Co due to TI layer shown in Figure 4f–h is crucial for SOT in TI/FM heterostructures where it has been considered[1] that applied current will be shunted through the metallic magnet and, therefore, not contribute to nonequilibrium spin density generation within the TI. On the contrary, Figure 4f–h and j–l suggests that the efficiency of SOT in TI/FM bilayers will be determined mainly by the topological proximity effect,[23,26] that is, the ability of the TI layer to induce sizable in-plane spin texture over the whole ultrathin FM layer. When current is passed parallel to MLs of Co hosting those proximity spin textures, they will generate a nonequilibrium spin density[14] $\mathbf{S}_{neq}$ and SOT[16,38] $\propto \mathbf{S}_{neq} \times \mathbf{m}$. We note that few previous experimental[26] and theoretical studies[23,26,40] have suggested possibility of proximity-induced spin textures but only within one monolayer of nonmagnetic metal or semiconductor in contact with TI layer and for special bonding requirements at the contact.[26]

We also find nontrivial in-plane spin texture even on the surface of Co in contact with vacuum, as shown in Figure 4b–d, which is nevertheless quite different from those in Figure 4f–h. The spin texture in Figure 4b–d is a consequence of the Rashba SOC enabled by inversion asymmetry due to Co surface[41] where an electrostatic potential gradient can be created by the charge distribution at the metal/vacuum interface and thereby confine wave functions into a Rashba spin-split quasi-2D electron gas.[42] The spin textures in Figure 4a–d explain the origin of recently observed[43] SOT in the absence of any adjacent heavy metal or TI layer.

DOI: 10.1021/acs.nanolett.7b02511
Nano Lett. 2017, 17, 5626−5633

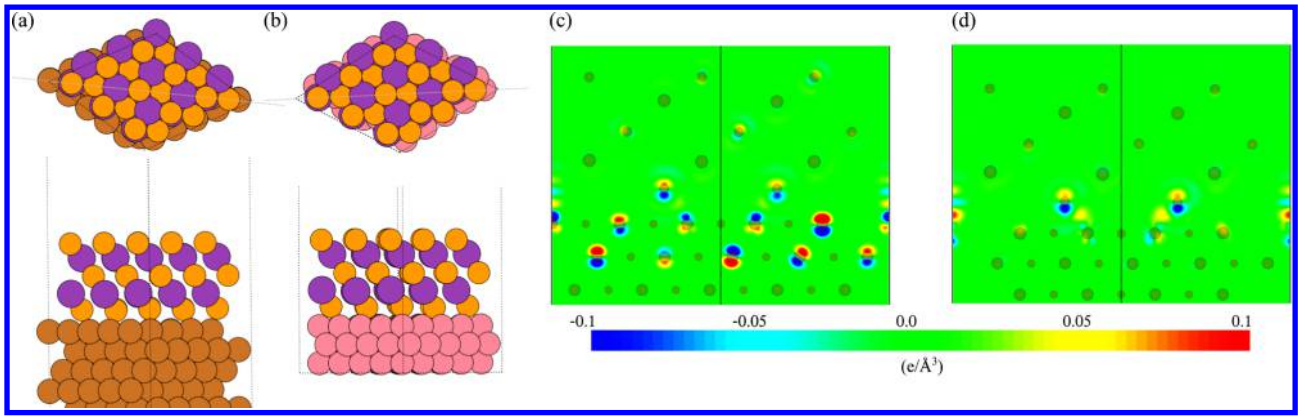

Figure 6. Top and side view of common unit cells for (a) Bi_2Se_3/Cu(111) and (b) Bi_2Se_3/Co(0001) bilayers. Panels c and d show charge rearrangement around the interface of bilayers in panels a and b, respectively.

Finally, we propose a purely charge transport measurement that could detect which among the spin-textures shown in Figure 3b–d resides at the Fermi level of TI/FM interface. Our scheme requires to fabricate vertical heterostructure in Figure 1b and measure its tunneling anisotropic magnetoresistance (TAMR). The TAMR is a phenomenon observed in magnetic tunnel junctions with a single FM layer[15,41,44,45] where SOC makes the band structure anisotropic so that the resistance of such junctions changes as the magnetization **m** is rotated by angle θ or ϕ in Figure 1b. The resistance change is quantified by the TAMR ratio defined as[41,45]

$$\mathrm{TAMR}_{\mathrm{out(in)}}(\alpha) = \frac{R(\alpha) - R(0)}{R(0)} \tag{6}$$

Here $\alpha \equiv \theta$ for $\mathrm{TAMR}_{\mathrm{out}}$ where magnetization in Figure 1b rotates in the plane perpendicular to the TI/FM interface, whereas $\alpha \equiv \phi$ for $\mathrm{TAMR}_{\mathrm{in}}$ where magnetization in Figure 1b rotates within the plane of the TI/FM interface. In the case of $\mathrm{TAMR}_{\mathrm{out}}(\theta)$, $R(0)$ is the resistance when $\mathbf{m} \parallel \hat{z}$ in Figure 1b; and in the case of $\mathrm{TAMR}_{\mathrm{in}}(\phi)$, $R(0)$ is the resistance when $\mathbf{m} \parallel \hat{x}$ in Figure 1b. Thus, $\mathrm{TAMR}_{\mathrm{out}}(\theta)$ changes due to the different orientations of the magnetization with respect to the direction of the current flow, while the situation becomes more subtle for $\mathrm{TAMR}_{\mathrm{in}}(\phi)$ where the magnetization remains always perpendicular to the current flow. Figure 5b demonstrates that the largest $\mathrm{TAMR}_{\mathrm{out}}(\theta = \pm 90^\circ)$ is obtained by tuning the Fermi level to $E_F - E_F^0 = -0.35$ eV so that nearly helical spin texture in Figure 3d resides at the Fermi level. Another signature of its presence is rapid increase of $\mathrm{TAMR}_{\mathrm{out}}(\theta)$ when tilting **m** by small angles θ away from the current direction. The in-plane $\mathrm{TAMR}_{\mathrm{in}}(\phi)$ shown in the inset of Figure 5b is much smaller (and difficult to converge in the number of transverse k-points) quantity which does not differentiate between spin textures shown in Figure 3b–d.

Methods. We employed the interface builder in the VNL[46] and CellMatch[47] packages to construct a common unit cells for (a) Bi_2Se_3(111)/Cu(111) bilayer, where the common unit cell is 5 × 5 in size compared to the smallest possible Cu(111) slab cell and copper is under compressive strain of 0.9% while Bi_2Se_3 lattice constant is unchanged; (b) Bi_2Se_3(111)/Co(0001) bilayer where Co(0001) has the same lattice constant as Bi_2Se_3, so the same unit cell as for Cu(111) is used without any strain on Co(0001). These two unit cells are illustrated in Figure 6a,b, respectively. In order to determine the best stacking of atomic layers and the distance of Bi_2Se_3 atoms with respect to surfaces of Cu(111) and Co(0001), we use DFT calculations as implemented in the VASP package.[48−50] The electron−core interactions are described by the PAW method,[32,51] and vdW-DF[52] with optB88 is used as density functional[53] in order to describe van der Waals (vdW) forces between QLs of Bi_2Se_3 or between Bi_2Se_3 and metallic layers. The cutoff energy for the plane wave basis set is 520 eV for all calculations, while k-points were sampled at 3 × 3 surface mesh. We use Cu and Co layers consisting of five MLs, where three bottom MLs are fixed at bulk positions while the top two metallic MLs closest to Bi_2Se_3 are allowed to fully relax until forces on atoms drop below 1 meV/Å. In order to avoid interaction with periodic images of the bilayer, 18 Å of vacuum was added in the z-direction.

For the case of Bi_2Se_3 on Co(0001), the most favorable position yields a binding energy of 460 meV per Co atom. Both ML of Co and QL of Bi_2Se_3 in direct contact gain some corrugation, roughly around ≃0.1 Å, while the average z-distance between them is 2.15 Å. The average distance between the ML of Cu and QL of Bi_2Se_3 in direct contact is around 2.26 Å with smaller corrugation than in the case of Co(0001), while the binding energy is 294 meV per Cu atom. For other relative positions of Bi_2Se_3 layer with respect to Cu(111) and Co(0001) layers the difference in binding energy is very small. Binding energies in both cases are rather small, thereby signaling the dominant vdW forces. Nevertheless, some charge rearrangement does occur at the interface due to push back/pillow effect,[54] as shown in Figure 6c,d where charge rearrangement is more pronounced for the case of Bi_2Se_3/Cu(111) interface.

The calculation of the retarded GF in eqs 1 and 3 requires $\mathbf{H}_{\mathbf{k}_\parallel}^{\mathrm{DFT}}$ represented in the linear combination of atomic orbitals (LCAO) basis set which makes it possible to spatially separate system into the active region attached to one or two semi-infinite leads, as illustrated in Figure 1a,b, respectively. We employ the ATK package[55] for pseudopotential-based LCAO noncollinear DFT calculations yielding $\mathbf{H}_{\mathbf{k}_\parallel}^{\mathrm{DFT}}$, from which we obtain retarded GFs and the corresponding spectral functions, as well as the resistance in eq 4. In ATK calculations, we use Perdew−Burke−Ernzerhof (PBE) parametrization of generalized gradient approximation for the exchange-correlation functional; norm-conserving pseudopotentials for describing electron−core interactions; and LCAO basis set generated by the OpenMX package[30,56] which consists of s2p2d1 orbitals on Co, Cu, and Se atoms, and s2p2d2 on Bi atoms. These

DOI: 10.1021/acs.nanolett.7b02511
Nano Lett. 2017, 17, 5626−5633

pseudoatomic orbitals were generated by a confinement scheme[30] with the cutoff radius 7.0 and 8.0 au for Se and Bi atoms, respectively, and 6.0 au for Co and Cu atoms. The energy mesh cutoff for the real-space grid is chosen as 75.0 hartree.

AUTHOR INFORMATION

Corresponding Author

*E-mail: bnikolic@udel.edu.

ORCID

Daniele Stradi: 0000-0002-3916-2168

Branislav K. Nikolić: 0000-0002-5793-7764

Notes

The authors declare no competing financial interest.

ACKNOWLEDGMENTS

We thank Takafumi Sato and Jia Zhang for insightful discussions. J.M.M.-T., K.D., P.-H.C., and B.K.N. were supported by NSF Grant ECCS 1509094 and DOE Grant DE-SC0016380. J.M.M.-T. also acknowledges support from Colciencias (Departamento Administrativo de Ciencia, Tecnologia e Innovacion) of Colombia. P.L. was supported by the Unity Through Knowledge Fund, Contract No. 22/15 and H2020 CSA Twinning Project No. 692194, RBI-T-WINNING. S.S., D.S., and K.S. acknowledge support from the European Commission Seventh Framework Programme Grant Agreement III−V-MOS, Project No. 61932 and Horizon 2020 research and innovation programme under Grant Agreement SPICE, project No. 713481. The supercomputing time was provided by XSEDE, which is supported by NSF Grant ACI-1053575.

REFERENCES

(1) Mellnik, A. R.; Lee, J. S.; Richardella, A.; Grab, J. L.; Mintun, P. J.; Fischer, M. H.; Vaezi, A.; Manchon, A.; Kim, E.-A.; Samarth, N.; Ralph, D. C. *Nature* **2014**, *511*, 449.

(2) Fan, Y.; Upadhyaya, P.; Kou, X.; Lang, M.; Takei, S.; Wang, Z.; Tang, J.; He, L.; Chang, L.-T.; Montazeri, M.; Jiang, G. Y.; Nie, T.; Schwartz, R. N.; Tserkovnyak, Y.; Wang, K. L. *Nat. Mater.* **2014**, *13*, 699.

(3) Wang, Y.; Deorani, P.; Banerjee, K.; Koirala, N.; Brahlek, M.; Oh, S.; Yang, H. *Phys. Rev. Lett.* **2015**, *114*, 257202.

(4) Fan, Y.; et al. *Nat. Nanotechnol.* **2016**, *11*, 352.

(5) Shiomi, Y.; Nomura, K.; Kajiwara, Y.; Eto, K.; Novak, M.; Segawa, K.; Ando, Y.; Saitoh, E. *Phys. Rev. Lett.* **2014**, *113*, 196601.

(6) Deorani, P.; Son, J.; Banerjee, K.; Koirala, N.; Brahlek, M.; Oh, S.; Yang, H. *Phys. Rev. B: Condens. Matter Mater. Phys.* **2014**, *90*, 094403.

(7) Jamali, M.; Lee, J. S.; Jeong, J. S.; Mahfouzi, F.; Lv, Y.; Zhao, Z.; Nikolić, B. K.; Mkhoyan, K. A.; Samarth, N.; Wang, J.-P. *Nano Lett.* **2015**, *15*, 7126.

(8) Rojas-Sánchez, J.-C.; Oyarzún, S.; Fu, Y.; Marty, A.; Vergnaud, C.; Gambarelli, S.; Vila, L.; Jamet, M.; Ohtsubo, Y.; Taleb-Ibrahimi, A.; Le Fèvre, P.; Bertran, F.; Reyren, N.; George, J.-M.; Fert, A. *Phys. Rev. Lett.* **2016**, *116*, 096602.

(9) Wang, H.; Kally, J.; Lee, J. S.; Liu, T.; Chang, H.; Hickey, D. R.; Mkhoyan, K. A.; Wu, M.; Richardella, A.; Samarth, N. *Phys. Rev. Lett.* **2016**, *117*, 076601.

(10) Kondou, K.; Yoshimi, R.; Tsukazaki, A.; Fukuma, Y.; Matsuno, J.; Takahashi, K. S.; Kawasaki, M.; Tokura, Y.; Otani, Y. *Nat. Phys.* **2016**, *12*, 1027.

(11) Hasan, M. Z.; Kane, C. L. *Rev. Mod. Phys.* **2010**, *82*, 3045.

(12) Qi, X.-L.; Zhang, S.-C. *Rev. Mod. Phys.* **2011**, *83*, 1057.

(13) Pesin, D.; MacDonald, A. H. *Nat. Mater.* **2012**, *11*, 409.

(14) Chang, P.-H.; Markussen, T.; Smidstrup, S.; Stokbro, K.; Nikolić, B. K. *Phys. Rev. B: Condens. Matter Mater. Phys.* **2015**, *92*, 201406.

(15) Mahfouzi, F.; Nagaosa, N.; Nikolić, B. K. *Phys. Rev. B: Condens. Matter Mater. Phys.* **2014**, *90*, 115432.

(16) Mahfouzi, F.; Nikolić, B. K.; Kioussis, N. *Phys. Rev. B: Condens. Matter Mater. Phys.* **2016**, *93*, 115419.

(17) Bansil, A.; Lin, H.; Das, T. *Rev. Mod. Phys.* **2016**, *88*, 021004.

(18) Soumyanarayanan, A.; Reyren, N.; Fert, A.; Panagopoulos, C. *Nature* **2016**, *539*, 509.

(19) Zhang, H.; Liu, C.-X.; Qi, X.-L.; Dai, X.; Fang, Z.; Zhang, S.-C. *Nat. Phys.* **2009**, *5*, 438.

(20) Luo, W.; Qi, X.-L. *Phys. Rev. B: Condens. Matter Mater. Phys.* **2013**, *87*, 085431.

(21) Lee, A. T.; Han, M. J.; Park, K. *Phys. Rev. B: Condens. Matter Mater. Phys.* **2014**, *90*, 155103.

(22) Zhao, E.; Zhang, C.; Lababidi, M. *Phys. Rev. B: Condens. Matter Mater. Phys.* **2010**, *82*, 205331.

(23) Hutasoit, J. A.; Stanescu, T. D. *Phys. Rev. B: Condens. Matter Mater. Phys.* **2011**, *84*, 085103.

(24) Soluyanov, A. A.; Gresch, D.; Wang, Z.; Wu, Q.; Troyer, M.; Dai, X.; Bernevig, B. A. *Nature* **2015**, *527*, 495.

(25) Sheng, X.-L.; Nikolić, B. K. *Phys. Rev. B* **2017**, *95*, 201402.

(26) Shoman, T.; Takayama, A.; Sato, T.; Souma, S.; Takahashi, T.; Oguchi, T.; Segawa, K.; Ando, Y. *Nat. Commun.* **2015**, *6*, 6547.

(27) Marzari, N.; Mostofi, A. A.; Yates, J. R.; Souza, I.; Vanderbilt, D. *Rev. Mod. Phys.* **2012**, *84*, 1419.

(28) Spataru, C. D.; Léonard, F. *Phys. Rev. B: Condens. Matter Mater. Phys.* **2014**, *90*, 085115.

(29) Zhang, J.; Velev, J. P.; Dang, X.; Tsymbal, E. Y. *Phys. Rev. B: Condens. Matter Mater. Phys.* **2016**, *94*, 014435.

(30) Ozaki, T. *Phys. Rev. B: Condens. Matter Mater. Phys.* **2003**, *67*, 155108.

(31) Narayan, A.; Rungger, I.; Sanvito, S. *Phys. Rev. B: Condens. Matter Mater. Phys.* **2012**, *86*, 201402.

(32) Blöchl, P. E. *Phys. Rev. B: Condens. Matter Mater. Phys.* **1994**, *50*, 17953.

(33) Velev, J.; Butler, W. *J. Phys.: Condens. Matter* **2004**, *16*, R637.

(34) Rungger, I.; Sanvito, S. *Phys. Rev. B: Condens. Matter Mater. Phys.* **2008**, *78*, 035407.

(35) Sørensen, H. H. B.; Hansen, P. C.; Petersen, D. E.; Skelboe, S.; Stokbro, K. *Phys. Rev. B: Condens. Matter Mater. Phys.* **2008**, *77*, 155301.

(36) Kim, J.; Sinha, J.; Hayashi, M.; Yamanouchi, M.; Fukami, S.; Suzuki, T.; Mitani, S.; Ohno, H. *Nat. Mater.* **2012**, *12*, 240.

(37) Nagaosa, N.; Sinova, J.; Onoda, S.; MacDonald, A. H.; Ong, N. P. *Rev. Mod. Phys.* **2010**, *82*, 1539.

(38) Haney, P. M.; Lee, H.-W.; Lee, K.-J.; Manchon, A.; Stiles, M. D. *Phys. Rev. B: Condens. Matter Mater. Phys.* **2013**, *87*, 174411.

(39) Checkelsky, J. G.; Ye, J.; Onose, Y.; Iwasa, Y.; Tokura, Y. *Nat. Phys.* **2012**, *8*, 729.

(40) Zhang, J.; Triola, C.; Rossi, E. *Phys. Rev. Lett.* **2014**, *112*, 096802.

(41) Chantis, A. N.; Belashchenko, K. D.; Tsymbal, E. Y.; van Schilfgaarde, M. *Phys. Rev. Lett.* **2007**, *98*, 046601.

(42) Bahramy, M.; King, P. D. C.; de la Torre, A.; Chang, J.; Shi, M.; Patthey, L.; Balakrishnan, G.; Hofmann, P.; Arita, R.; Nagaosa, N.; Baumberger, F. *Nat. Commun.* **2012**, *3*, 1159.

(43) Emori, S.; Nan, T.; Belkessam, A. M.; Wang, X.; Matyushov, A. D.; Babroski, C. J.; Gao, Y.; Lin, H.; Sun, N. X. *Phys. Rev. B: Condens. Matter Mater. Phys.* **2016**, *93*, 180402.

(44) Park, B. G.; Wunderlich, J.; Williams, D. A.; Joo, S. J.; Jung, K. Y.; Shin, K. H.; Olejník, K.; Shick, A. B.; Jungwirth, T. *Phys. Rev. Lett.* **2008**, *100*, 087204.

(45) Matos-Abiague, A.; Fabian, J. *Phys. Rev. B: Condens. Matter Mater. Phys.* **2009**, *79*, 155303.

(46) Virtual Nanolab (VNL) 2016.4, http://www.quantumwise.com (accessed August 1, 2017).

(47) Lazić, P. *Comput. Phys. Commun.* **2015**, *197*, 324.

DOI: 10.1021/acs.nanolett.7b02511
Nano Lett. 2017, 17, 5626−5633

(48) Vienna Ab initio Simulation Package (VASP) 5.4, https://www.vasp.at (accessed August 1, 2017).
(49) Kresse, G.; Hafner, J. *Phys. Rev. B: Condens. Matter Mater. Phys.* **1993**, *47*, 558.
(50) Kresse, G.; Furthmüllerb, J. *Comput. Mater. Sci.* **1996**, *6*, 15.
(51) Kresse, G.; Joubert, D. *Phys. Rev. B: Condens. Matter Mater. Phys.* **1999**, *59*, 1758.
(52) Dion, M.; Rydberg, H.; Schröder, E.; Langreth, D. C.; Lundqvist, B. I. *Phys. Rev. Lett.* **2004**, *92*, 246401.
(53) Mittendorfer, F.; Garhofer, A.; Redinger, J.; Klimeš, J.; Harl, J.; Kresse, G. *Phys. Rev. B: Condens. Matter Mater. Phys.* **2011**, *84*, 201401.
(54) Vázquez, H.; Dappe, Y. J.; Ortega, J.; Flores, F. *J. Chem. Phys.* **2007**, *126*, 144703.
(55) Atomistix ToolKit (ATK) 2016.4, http://www.quantumwise.com (accessed August 1, 2017).
(56) OpenMX 3.8, http://www.openmx-square.org (accessed August 1, 2017).

DOI: 10.1021/acs.nanolett.7b02511
Nano Lett. 2017, 17, 5626−5633